Reducing subjectivity in EIS interpretation of corrosion and corrosion inhibition processes by in-situ optical analysis

Denissen, Paul J.; Garcia, Santiago J.

DOI
10.1016/j.electacta.2018.10.018

Publication date
2019

Document Version
Final published version

Published in
Electrochimica Acta

Electrochimica Acta 293 (2019) 514–524

Contents lists available at ScienceDirect

Electrochimica Acta

journal homepage: www.elsevier.com/locate/electacta

Reducing subjectivity in EIS interpretation of corrosion and corrosion inhibition processes by in-situ optical analysis

Paul J. Denissen*, Santiago J. Garcia**

Novel Aerospace Materials Group, Faculty of Aerospace Engineering, Delft University of Technology, Kluyverweg 1, 2629 HS Delft, the Netherlands

ARTICLE INFO

Article history:
Received 29 August 2018
Received in revised form
2 October 2018
Accepted 3 October 2018
Available online 4 October 2018

Keywords:
AA2024
Corrosion inhibition
Cerium
DMTD
DEDTC
2-MBT
Lithium
8HQ

ABSTRACT

An in-situ hyphenated optical and electrochemical method for the real-time study of corrosion and corrosion inhibition processes is presented and validated for the case of AA2024-T3 exposed to two NaCl concentrations and six inhibitors. During testing, 5 μm resolution optical images of the exposed surface are obtained in parallel to electrochemical impedance measurements using a home-made 3D printed electrochemical cell. This method allowed obtaining both optical and electrochemical information of the studied surface with high time correlation. A data treatment analysis of the optical images was established thereby allowing the identification and quantification of corrosion-features related to intermetallic corrosion (e.g. trenching and meta-stable pitting) and co-operative corrosion (e.g. corrosion-rings, domes and surface-oxides) on a spatiotemporal scale, generally only observed through the use of ex-situ methods such as SEM. In addition, the study of the long-term corrosion inhibition of six inhibitors at concentrations ranging from 10^{-3} M to 10^{-6} M allowed quantifying inhibition kinetics as well as identifying different inhibitor and concentration dependent mechanisms (e.g. Cerium and DEDTC vs. Lithium) and decreasing incongruences between impedance and inhibition behaviour (e.g. DMTD). As a result, the use of quantifiable in-situ optical analysis is confirmed as a powerful tool to better interpret electrochemical signals or monitor electrochemical-dependent surface phenomena.

1. Introduction

Electrochemical Impedance Spectroscopy (EIS) is a well-established technique broadly used to monitor corrosion processes and monitor coating properties [1]. The foundation for EIS dates back to the end of the 19th century by Oliver Heaviside who applied Laplace transformations to frequency dependent electrical circuits, thereby enabling the conversion of integro-differentials to simple algebraic equations [2]. His paper, published in 1872, was heavily criticized because the theorem could not be proven mathematically until the following century [3]. It was not until the 1980s that EIS awoke the general interest of scientists working on coatings, corrosion and batteries, rapidly growing from around 30 annual publications in 1980 to more than 6000 in 2017 [1]. Despite the ever increasing literature, effective interpretation of EIS data is not always evident for complicated systems that require mathematical skills and good understanding of the involved physical processes [4].

As a natural evolution, EIS data is often interpreted through electrical equivalent circuits (EECs) whereby a successful fit is described as proof that the presented physical model is correct, while in fact many different models within the same accuracy will represent the data equally well [5]. The correctness of the EECs can only be truly confirmed by applying a dataset of infinite accuracy to the model, which is clearly an unrealistic presumption. Part of the problem lies in the fact that electrochemical processes are often complex and are influenced by many different parameters such as composition, porosity, interphases, environmental conditions and sample geometry, as well as the time superposition of different phenomena [6–9]. These factors increase subjectivity and risk of misinterpretations difficult to identify. In the case of corrosion and coating studies, a common approach to interpret electrochemical data is to perform analysis by means of optical microscopy [10] and other surface analysis techniques such as TEM [11], SEM-EDS [12], Raman [13] and FTIR [14]. Despite informative, this approach requires the sample to be extracted from the electrolyte, analysed and in some cases brought back to the electrochemical test, thereby

* Corresponding author.
** Corresponding author.
E-mail addresses: p.j.denissen@tudelft.nl (P.J. Denissen), s.j.garciaespallargas@tudelft.nl (S.J. Garcia).

https://doi.org/10.1016/j.electacta.2018.10.018

missing the time-dependent information relevant to interpret time-evolution of electrochemical signals as well as their correlation to macroscopic phenomena simultaneously. Alternatively, multiple samples can be collected and analysed after different immersion times but raise concerns on the influence of the different intermetallic (IM) distribution or composition between the samples on the optical analysis and electrochemical signals [15]. As an alternative to these traditional approaches some authors working on coatings and corrosion have coupled electrochemical measurements to other techniques (e.g. X-ray micro-tomography [16,17], Atomic Emission Spectroelectrochemistry [18] and Raman Spectroscopy [19]) to monitor corrosion phenomena in real time. Despite offering powerful information about corrosion processes and delamination of coatings, such techniques remain scarcely used due to their limited availability, complexity and high costs.

In this paper we propose a simple and inexpensive method to obtain real-time electrochemical and optical information of the corrosion process of metals immersed in electrolyte. The hyphenated optical and electrochemical setup and the data analysis protocol here presented allow obtaining a full set of characteristic parameters to monitor and study the evolution of surface-related macroscopic phenomena and their correlation to electrochemical data with spatio-temporal resolution. The setup and data processing protocol are defined and validated by studying the corrosion behaviour of aluminium alloy 2024-T3 exposed to 0.05 M and 0.5 M NaCl solutions. For this, the electrochemical changes observed in the EIS spectra are related to the corresponding macroscopic surface changes observed with the optical component and the interpretation validated by means of previous works on the corrosion process of AA2024-T3 [20–36]. Subsequently, the optical-electrochemical setup is employed to study the time-dependent inhibiting efficiency of six corrosion inhibitors for AA2024-T3 alternative to chromates at inhibitor concentrations ranging from 10^{-3} M to 10^{-6} M. The six inhibitors were selected based on their nature, protection efficiency, and reportedly different inhibiting mechanisms. Cerium Nitrate ($Ce(NO_3)_3$) and Lithium Carbonate (Li_2CO_3) were selected as efficient inorganic corrosion inhibitors, while Sodium diethyldithiocarbamate trihydrate (DEDTC), 2,5-dimercapto-1,3,4-thiadiazolate (DMTD), 2-mercaptobenzothiazole (2MBT), and 8-hydroxyquinoline (8HQ) were selected as organic corrosion inhibitors. While the inhibitor mechanism for Ce [37] and Li [38,39] are known, this remains an ongoing debate for the selected organic inhibitors. These have been reported to act as insoluble chelating reagents, specifically at cathodic copper-rich regions [40], or work as mixed type inhibitors that chemisorb [41] over the entire surface. This paper shows the validity of the optical-electrochemical in-situ evaluation as a powerful approach to visualize and quantify surface phenomena related to the corrosion or/and inhibition processes normally observed by ex-situ post-mortem SEM studies, leading to a better interpretation of corrosion-related processes.

2. Materials and methods

2.1. Materials

Commercial 2 mm thick bare AA2024-T3 sheets were obtained from Kaizer Aluminium and cut into coupons of 25 × 50 mm. The native oxide layer was removed by Scotch Brite 3 M followed by degreasing with acetone and rinsing with demineralised water prior to clamping in the optical-electrochemical cell and exposure to NaCl electrolyte solutions with and without corrosion inhibitors.

Analytical grade corrosion inhibitors were purchased from Sigma-Aldrich and used as received: Cerium Nitrate Hexahydrate ($Ce(NO_3)_3$, >99%), Lithium Carbonate (Li_2CO_3, >99%), Sodium diethyldithiocarbamate trihydrate (DEDTC, >97%), 2,5-dimercapto-1,3,4-thiadiazolate (DMDT >99%), 2-mercaptobenzothiazole (2-MBT, >98%), and 8-hydroxyquinoline (8HQ, >99%). Sodium chloride (NaCl, >98%) was purchased from VWR Chemicals. Aqueous solutions at 0.05 and 0.5 M NaCl were prepared using Milipore® Elix 3 UV filtered water. The inhibitors were then added to the 0.05 M NaCl aqueous solution to obtain varying corrosion inhibitor concentrations in the range 10^{-3} M to 10^{-6} M.

2.2. Optical and electrochemical in-situ measurement

A potentiostat Metrohm PGSTAT 302 fitted with FRA32 M and MUX. MULTI.4 modules was used to perform the Electrochemical Impedance Spectroscopy (EIS) and Open Circuit Potential (OCP) measurements. A three-electrode set up was employed consisting of a silver/silver-chloride (Ag/AgCl) reference electrode (RE), 6.6 mm diameter graphite rod as counter electrode (CE) and the metallic coupons subject of study acting as the working electrodes (WE). The frequency range of study was 10^{-2}-10^{5} Hz at 10 points per decade, with applied amplitude of 10 mV root mean square (RMS) over OCP to minimize the influence of the test on the metal-coating system while still obtaining a reliable response. The potentiostat was controlled with a USB interface through the software package NOVA V1.11.1 to allow for automatic EIS measurements every hour. For the optical measurement an inexpensive and commercially available USB Celestron handheld digital microscope camera with 5.0 megapixel resolution and equipped with an adjustable 8-led ring-light was used. The camera was programmed to take a picture every 10 min in parallel with the EIS measurements.

A home-made cell was produced from polycarbonate using an Ultimaker 2+ 3D printer for the real time optical and electrochemistry studies as shown in Fig. 1 and support information (SI) 1.

The cell shown in Fig. 1b was subsequently cleared of printing defects and coated with epoxy/amine coating to avoid leakage. A 3 mm thick transparent polymethylmethacrylate (PMMA) lid was attached to the previously manufactured aperture of 40 mm diameter to act as window for the optical camera placement. The metallic coupons subject of study (in this case AA2024-T3) were then placed, with the help of a copper block, against a 9.5 mm diameter hole at the opposite side of the window for the optical analysis as shown in Fig. 1. The optical camera and ring-light was then aligned against the PMMA window focusing it to the metal surface. Both the camera and the electrochemical cell were placed inside a fully closed Faraday cage to avoid external electrochemical and optical interferences. Right before immersion of the three-electrode setup the cell was filled with 100 mL electrolyte solution.

2.3. Optical analysis

Quantitative information extracted from the in-situ optical analysis was obtained through an automated image analysis procedure as shown in Fig. 2.

The camera-software recorded and automatically stored images in 8-bit format (256 bin grey-scale, bin 0 for black and bin 255 for white) right from the start of the measurement. In order to compensate for changes in contrast/brightness caused by differences in lightning and auto-exposure settings of the camera between images a calibration sticker containing 5 grey standards including a scale bar was attached to the metal surface prior to immersion as shown in Fig. 2a. In order to obtain quantifiable information from the images an evaluation protocol was established. A Macro scripting protocol was used to automatically analyse the images in ImageJ open source software (SI 2). The calibration-script measures the grey-value on the calibration sticker for each

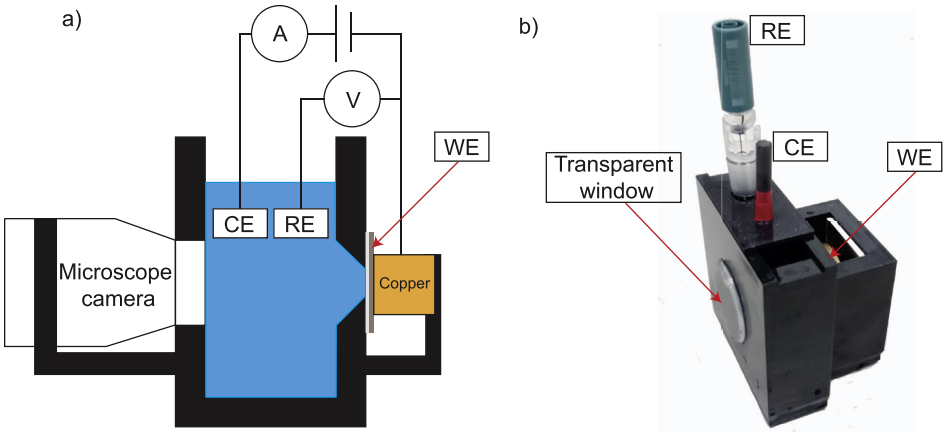

Fig. 1. Schematic illustration of the cell for the optical and electrochemical studies (a). Scheme shows the three-electrode set up and the position of the microscope optical camera with respect to the working electrode target of the study. Photography of the optical-electrochemical cell used in this study (b).

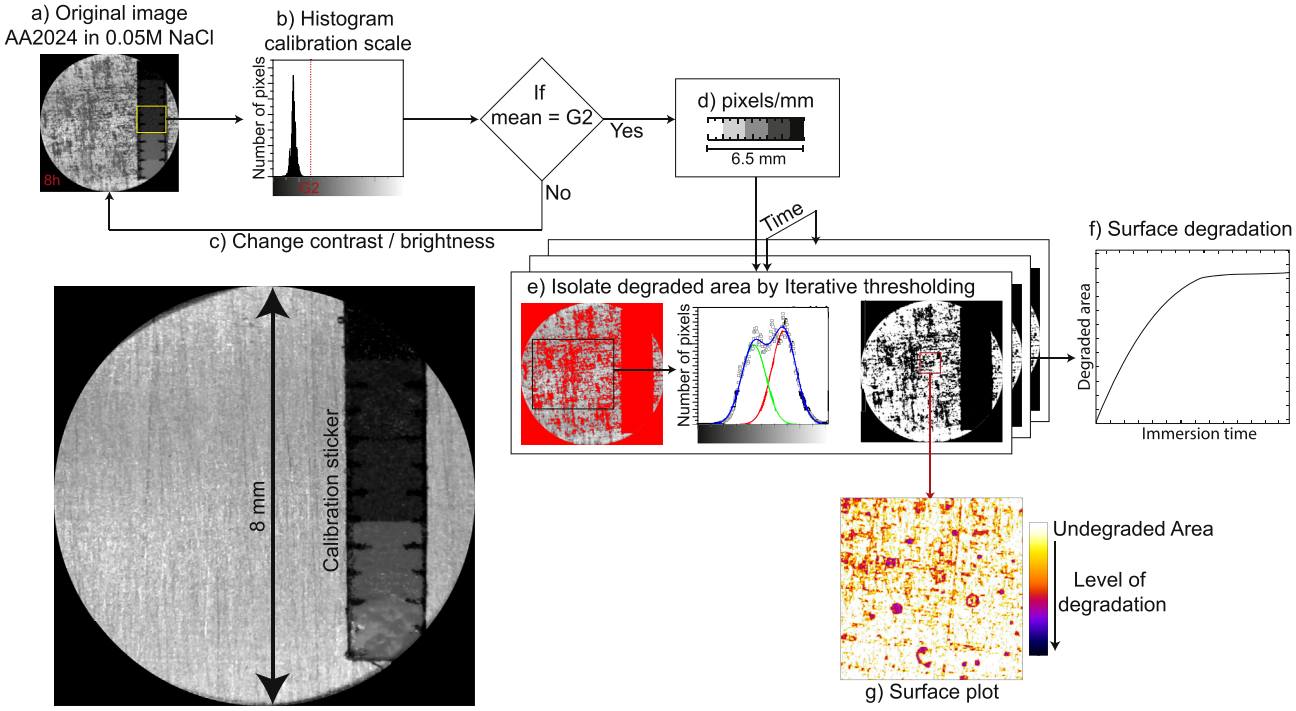

Fig. 2. Block-diagram of the image analysis procedure.

individual image (Fig. 2b) and adjusts iteratively the contrast/brightness of the image until the grey-value of the calibration sticker matches their predefined calibrated standard value (Fig. 2c), thereby also correcting the corresponding metal surface to any optically imposed external interference. The scale-bar on the calibration sticker was further used by the script to accurately determine the magnification of the images (Fig. 2d), which was around 5 μm per pixel for all the measurements. For easier processing, all images corresponding to one test were stacked together and the averaged 8-bit histogram over the entire exposure-time was calculated (Fig. 2e). This allowed obtaining a double-Gaussian distribution whereby the peak in the light regime is attributed to the pixels corresponding to non-corroded aluminium surface (background) and the peak in the dark regime (foreground) to the pixels corresponding to optically detectable macroscopic phenomena related to the corrosion processes (e.g. pitting corrosion, intergranular corrosion and deposits on the surface which are darker than the background such as oxides). To separate the signals corresponding to the corrosion-related optically detectable features from the unaffected background an iterative thresholding algorithm developed by Ridler and Calvard [42] was implemented to deconvolute the two peaks in the histogram, as expressed by Equation (1) and the procedure described here below;

$$\theta_i = \frac{m_{f,i-1} + m_{b,i-1}}{2} \quad untill\ \theta_i = \theta_{i-1} \tag{1}$$

where (θ) is the starting grey value at half of the dynamic range used as threshold to segment the total histogram into two parts. Then, the mean grey values were computed for both parts, namely

the foreground (m_f) and background (m_b). The average of these two parts represents the new threshold and the entire calculation process is repeated 'i' number of times until the threshold converges to its optimal value. For each individual image the pixels with grey-values below this threshold were assigned as corresponding to the unaffected background and converted to white. The image was then reconstructed into 8-bit whereby the optically-detectable time dependent surface features receive a grey-value between 1 and 255. These now highlighted areas are then used to quantify what is here presented as the degraded area (Fig. 2f). The degree and type of degradation processes was further analysed by constructing a colour-plot whereby the grey-value of each pixel was transposed to a colour-gradient (Fire-LUT) in which the pixels related to no corrosion (white) are coloured white and the pixels related to high degradation (black) are coloured purple (Fig. 2g). Such an approach allowed identifying in a first order approximation surface features as pits or as oxides depending on the colour scale.

3. Results and discussion

3.1. Identification of corrosion-related features in AA2024-T3

3.1.1. Global temporally-resolved evaluation

Fig. 3 shows the electrochemical (Bode plots) and optical grey-scale images obtained with the optical-electrochemical set-up for AA2024-T3 panels after 1 h, 3 h, 9 h and 15 h immersion in 0.05 M NaCl and 0.5 M NaCl solutions. A movie of the optically recorded images can be found in SI 3.

The effect of the salt concentration is clearly visible both electrochemically and optically (Fig. 3) while the time-dependent effects are only clearly visible in the optical results. At high frequencies between 100 and 1000 Hz the influence of fast electron-transfer results in a lower total impedance and higher phase for the highest salt concentration as expected for higher electrolyte conductivity [20]. At frequencies between 1 Hz and 0.01 Hz the total impedance and phase shift can be attributed to electrochemical processes near the metal surface (e.g. oxide layers) [21–23]. Kramers-Kronig residual errors on the data (shown in SI 4) confirmed the systems instability during the first 2–6 h of immersion at frequencies below 1 Hz. Such electrochemical instabilities are also related to large OCP fluctuations as a result of pitting, causing unrealistic EIS data [24]. The unprocessed greyscale images for the first immersion hours could also not confirm the presence of such surface-changes due to a lack of resolution in the current setup. After the first hours of immersion the fluctuations below 0.05 Hz become lessened together with an increasing negative phase angle. This, combined with the reduction of the total impedance at 0.01 Hz indicates the appearance of another time constant below the investigated frequency region and correspond to the mass-transfer diffusion processes located at the pits [25].

In order to obtain more detailed and quantifiable information of the surface-related corrosion processes, the electrochemical and optical data were further analysed as explained in the methods section. The impedance values at 0.01 Hz were selected for the comparison as this frequency highlights the on-going processes at the metal surface related to corrosion phenomena [43]. Fig. 4 shows the time-evolution in electrolyte of: (a, b) the total impedance |Z| at a frequency of 0.01 Hz for AA2024-T3; and (c, d) the calculated optically-detectable degraded area in percentage.

From Fig. 4 a clear increase of the degraded area and decrease of the total impedance with the immersion time can be observed for both electrolyte salt concentrations. The evolution in total impedance shows a high degree of scatter between the repeating tests and is fairly similar at both salt concentrations. Contrarily, the surface degradation quantified from the optical images evolves significantly faster at higher salt concentrations (0.5 M NaCl) and shows good reproducibility by the narrower error-band. Three different stages of the surface corrosion process can be identified and related to the corrosion features reported in literature for AA2024-T3 as a first order approximation:

(I) First 2 and 4 h of immersion in 0.5 M and 0.05 M NaCl, respectively: slow increase of the degraded area until it reaches 7% degraded area (Fig. 4c and d) combined with a limited amount of stable total impedance measurements at 0.01 Hz (instable unreliable data with negative phase angle and in accordance to large Kramers-Kronig residual errors (SI 4) are not shown). This is in agreement with the first stages of the corrosion process where chloride ions break down the visually undetectable natural oxide layer [26] explaining the higher impedance measured during the initial hours of immersion followed by the decrease over time as shown in Fig. 4a. While the optical changes during the first hours of immersion where difficult to detect from the unprocessed grey-scale images (Fig. 3), the optical analysis procedure used to calculate the surface-changes (Fig. 4c and d) clearly shows an increase of degraded-area due to localised pitting corrosion occurring first at isolated S-phase intermetallic (IM) particles followed by AlCuFeMn and $(AlCu)_x$ $(FeMn)_ySi$ (IM) particles [15]. The reason for the initiation at the S-phase is due to their lower OCP compared to other IM particles and matrix, making them anodically active thereby undergoing dissolution and trenching [27,28]. Several studies report that this corrosive attack occurs during the first minutes of immersion at the sub-micron level in the form of dissolution and copper enrichment of the S-phase until they switch to cathodic sites, resulting in the dissolution of hydrated aluminium oxide products [15,29,30]. Boag et al. also illustrate in their work that these oxides might appear on the S-phase and form a homogeneous layer with limited lifetime over the entire IM/matrix interface during the first hours of immersion, which can electrochemically isolate the IM particle remnants. Even if many of these individual corrosion-processes take place below detection-limit of the current optical setup, the total accumulation of degraded-area around 7% is in good correlation with trenching, pit-initiation, and the formation of an oxide products on and around the IM particles that cover roughly 3% of the total area on AA2024 [31].

(II) From 2 to 6 h and 4–12 h immersion in 0.5 M and 0.05 M NaCl, respectively: comparable decrease of total impedance of roughly 0.5 $(k\Omega\,cm^2)$/h (Fig. 4a and b) for the two salt concentrations, combined with an increase in degraded area of 10%/h for 0.5 M NaCl and 5%/h for 0.05 M NaCl (Fig. 4c and d). This second stage of surface corrosion corresponds to co-operative corrosion or severe corrosion attack reported in literature [32,33]. This process involves a number of particles, as the name indicates, and describes the broader interaction of IM particles with themselves, the wider matrix or both.

(III) From 6 to 12 h onwards in 0.5 M and 0.05 M NaCl, respectively: decrease of the degraded area growth kinetics (less visible for 0.05 M) combined with stagnation of the total impedance in the case of 0.5 M. The final stabilization of total impedance and decrease of the degradation rate is most likely caused by the decrease of surface corrosion combined

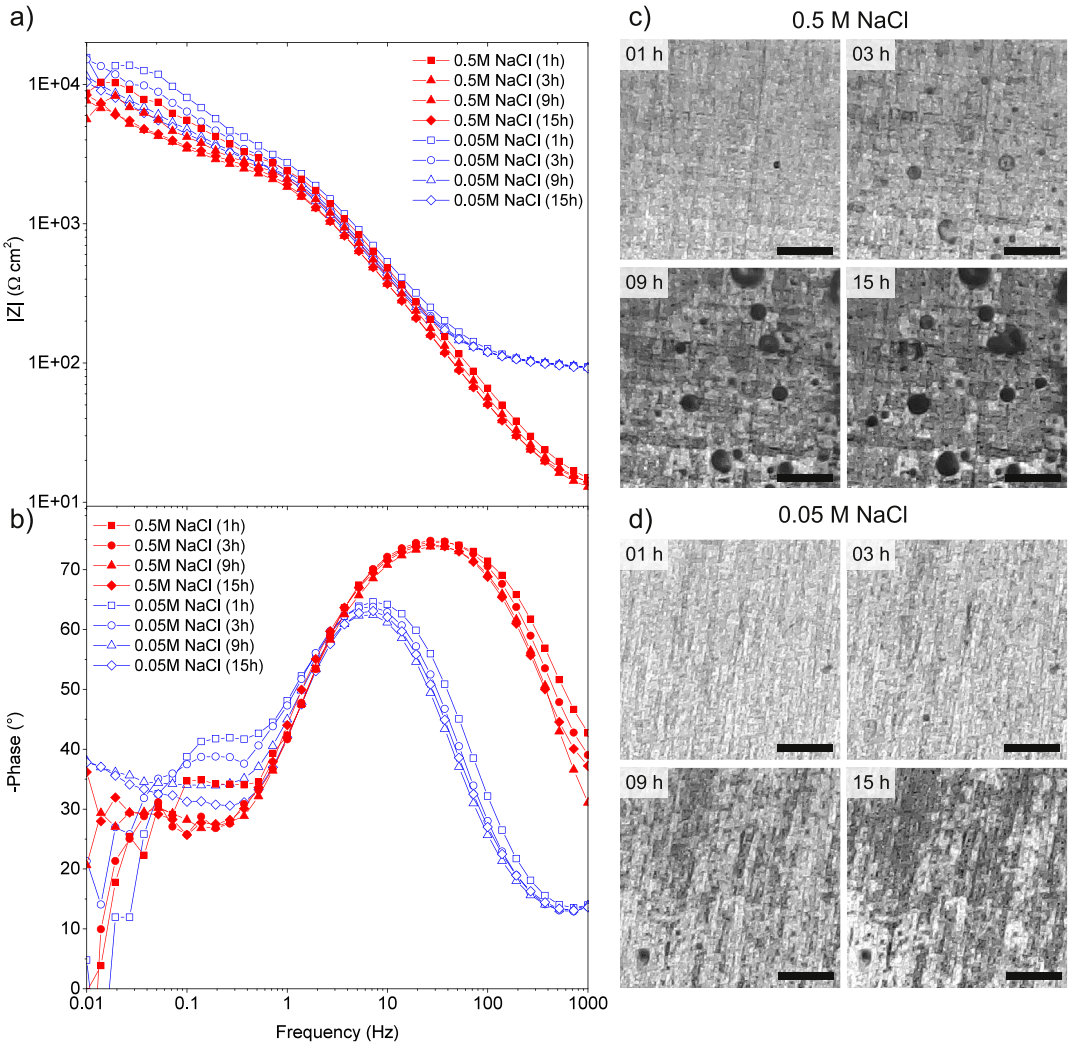

Fig. 3. Bode plots of AA2024-T3 exposed to 0.5 M and 0.05 M NaCl and corresponding optical images where (a) shows the total impedance |Z| and (b) the phase angle after 1 h, 3 h, 9 h and 15 h immersion. (c) and (d) show the corresponding optical images to the selected EIS times for 0.5 M and 0.05 M NaCl, respectively. Scale bar represents 500 μm.

with the propagation to subsurface corrosion attack as reported in literature [10].

3.1.2. *Local spatial-resolved evaluation*

In order to shed some extra light on the local surface corrosion phenomena, colour-plots of the optical images were derived as for the 0.05 M NaCl solution in Fig. 5.

Multiple yellow spots of 5–20 μm diameter appear during the first 30 min immersion and are related to pit initiation involving trenching. The size and distribution of these spots are in good agreement with the reported average size for IM particles found in AA2024, which are evenly distributed and have cross-sectional diameters between 1 and 30 μm [34]. Between 1 and 3 h immersion the growth of these spots is in good agreement with further IM dissolution and trenching. The thin yellow border around grey areas (IMs) suggests higher depth and a higher degree of degradation related to the propagation of meta-stable pits possibly caused by the deposition of the thin copper layer around the pits and trenching sites [35]. Besides the growth, the micrographs show that the active locations start interconnecting to each-other to form faint rings of corrosion-products with a size between 50 and 200 μm and coincide with the descriptions made for early-stage co-operative corrosion [36]. After 3 h the local surface-degradation at the meta-stable pits and corrosion-rings start to coalesce into dense circular spots that appear purple in colour which can be typified as domes of corrosion products as indicated in Fig. 5 (6 h) [36]. The surface around the domes has degraded significantly as well, suggesting an increase of oxide-deposits at the surface. After 6 h of immersion the amount of oxide-deposits continues to increase (presence of domes), suggesting the propagation to subsurface corrosion under the domes [36] besides the propagation of surface corrosion attack.

The detection of surface-related features in time under immersion conditions as obtained here and their relation to reported local corrosion activity around the IM particles and co-operative sites can be summarised as shown in Fig. 6 for AA2024-T3 in 0.05 M NaCl. Fig. 6 shows that the in-situ spatiotemporal optical analysis makes it possible to observe and identify several different corrosion-features typically only identified by SEM or ex-situ

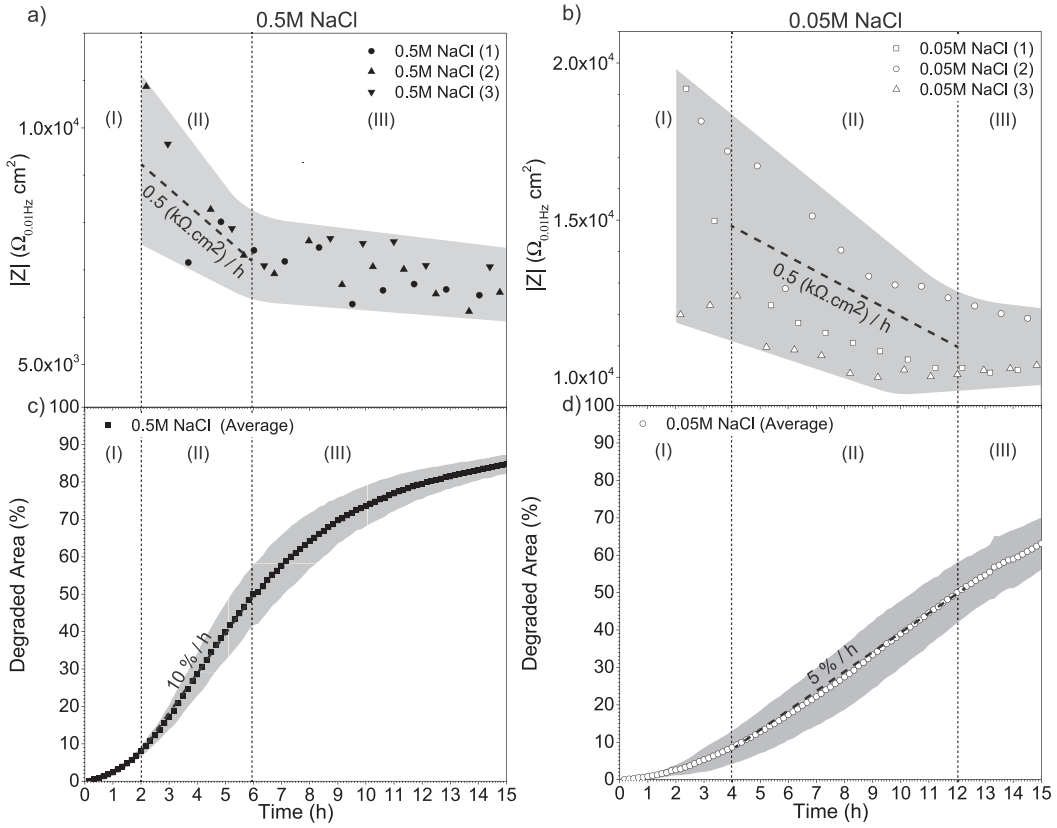

Fig. 4. Processed optical and electrochemical data into quantifiable information for AA2024-T3 immersed in 0.5 M and 0.05 M NaCl. (a, b) Shows the time-evolution of the stable total impedance |Z| at a frequency of 0.01 Hz in and with negative phase angle; and (c, d) time-evolution of the optically detectable degradation area. Note: greyscale bands show the error bars related to three repeated tests, and the numbers relate to the different stages of the corrosion process.

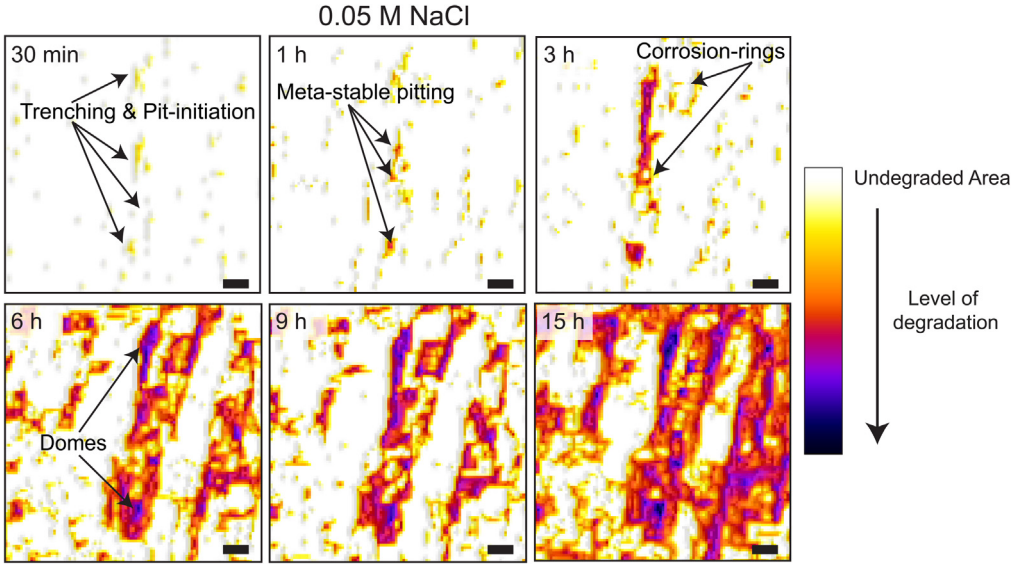

Fig. 5. Colour-plots of the micrographs of the same region after different immersion-times in 0.05 M NaCl. Scale bars represent 50 μm. (For interpretation of the references to colour in this figure legend, the reader is referred to the Web version of this article.)

optical microscopy studies [11,15,29,32]. While the current optical setup with 5 μm pixel resolution does not allow the observation of early-stage etching, quantification of the IM composition or sub-surface related processes (e.g. subsurface intergranular attack), the different features related to corrosion around IM particles (i.e. trenching and meta-stable pitting) and co-operative corrosion (i.e. corrosion rings, domes, and surface oxide-deposits) can easily be identified and quantified based on their time-evolved kinetics and colour map of the optical images while the electrochemical signals are of more difficult correlation to macroscopic phenomena.

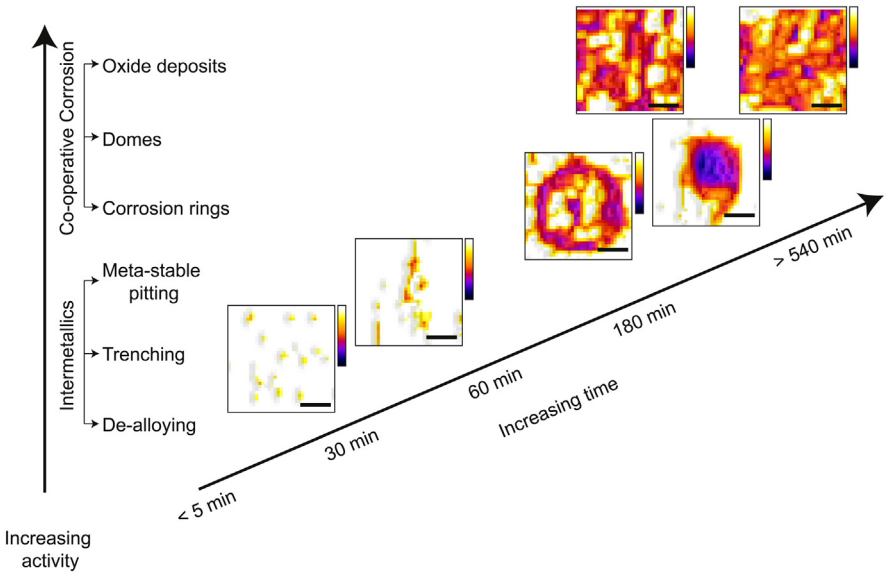

Fig. 6. Summary of the optical observations for the evolution of intermetallic and co-operative corrosion on the surface of AA2024-T3 in 0.05 M NaCl. Scale bars represent 50 μm. (For interpretation of the references to colour in this figure legend, the reader is referred to the Web version of this article.)

3.2. Evaluation of corrosion inhibitors

3.2.1. Global temporally-resolved evaluation

The corrosion protection potential of AA2024-T3 by six different salts at concentrations ranging from 10^{-3} M to 10^{-6} M was studied with the optical-electrochemical setup. The Nyquist and Bode plots of six different inhibitors in 0.05 M NaCl solutions after 15 h of immersion can be found in SI 5. While each inhibitor shows a particular trend depending on their concentration and inhibition mechanism, information on the degree of protection remains difficult to obtain. Moreover, inhibition effects are often identified by the impedance values at low frequencies (e.g. 0.01 Hz) as inhibition is often related to the suppression of electron transfer due to the formation of a passivation layer on the metal surface or IM locations [37]. As a consequence we propose the combination of optical and electrochemical data as presented in Fig. 7, showing the total impedance |Z| at a frequency of 0.01 Hz together with the calculated optically-detectable degraded area in percentage for an easier interpretation and quantification of the inhibition effects.

Fig. 7 shows that the total impedance values at 0.01 Hz remain relatively similar during 15 h of immersion, while the optical degradation shows either no changes or a clear increase over time depending on the degree of inhibition. Three different overall inhibitor behaviours can be identified based on their impedance and degraded area time evolution: (i) Ce, DEDTC, 2MBT and 8HQ; (ii) Li; and (iii) DMTD. Inhibitors Ce, DEDTC, 2MBT and 8HQ at concentrations between 10^{-3} M and 10^{-4} M show higher $|Z|_{0.01Hz}$ than the non-inhibited sample (named 0.05 NaCl). This coincides with less than 1%/h degraded area evolution during 15 h of immersion At 10^{-5} M inhibitor concentration only Ce continues the trend of high impedance and low degraded area (Fig. 7a) thereby still showing good protection and inhibitor robustness. At such inhibitor concentrations the three organic inhibitors (DEDTC, 2MBT and 8HQ) show similar/lower impedance values at 0.01 Hz than the non-inhibited sample combined with an increase of the degraded surface-area between 2%/h and 5%/h, similar to the values shown for the non-inhibited sample in Fig. 4d, thereby suggesting a loss of their inhibiting power at low concentrations (Fig. 7 b-d).

Li inhibitor on the other hand shows an abrupt transition in the impedance time evolution as function of the inhibitor concentrations at around 10^{-3} M (Fig. 7e). In this case, the impedance values at 0.01 Hz for all the tested concentrations are close to the values for the non-inhibited sample suggesting high local corrosion attack. Interestingly, at 10^{-3} M the degradation profile changes and shows a very fast overall corrosion attack (almost complete surface degradation) within 1 h which is kept during the first 6 h of immersion to start decaying afterwards. This suggests a significant loss of material, followed by a second transition after 6 h whereby the surface gradually becomes comparable (optically) to its initial state suggesting a passivation of the surface. These results can be related to observations found in literature for this particular inhibitor [38,39]. The initial surface-degradation during the first 6 h can be related to massive surface etching of the aluminium surface, whereby the presence of Li-inhibitor promotes the corrosion processes at the surface and results in the dissolution of aluminium into an amorphous $Al(OH)_3$. This is further supported by the low-frequency impedance values comparable to those of the non-inhibited sample suggesting no passivation-layer has been formed yet during this period. After 6 h the amount of degraded area decreases along with a slight increase of impedance (Fig. 7b). This suggests that an electrochemically passive barrier is being developed and is in good agreement with the reported works showing the formation of a protective hydrated lithium/aluminium layer [38,39]. From the results in Fig. 7b it can be seen that this protective barrier layer is not formed when lower inhibitor concentrations are used ($<10^{-3}$ M) and might in some cases lead to massive local degradation of the exposed surface.

In the case of DMTD, low concentrations (10^{-5} and 10^{-6} M) show higher impedance values than the reference non-inhibited solution accompanied by very low surface degradation (below 1%/h). Nevertheless, high concentrations (10^{-3} and 10^{-4} M) show similarly low surface degradation but lower impedance values than the reference non inhibited sample suggesting an incongruence between the two results. The misleading low impedance values can be attributed to the so called pseudo-inductance process ascribed to the relaxation effects of ionic adsorption/desorption phenomena at the electrode surface which become more prominent at high concentrations [44]. The Nyquist plot for DMTD (10^{-3} and 10^{-4} M) as shown in SI 5 confirms that this pseudo-inductance occurs for this inhibitor by the depressed semicircle at low frequencies

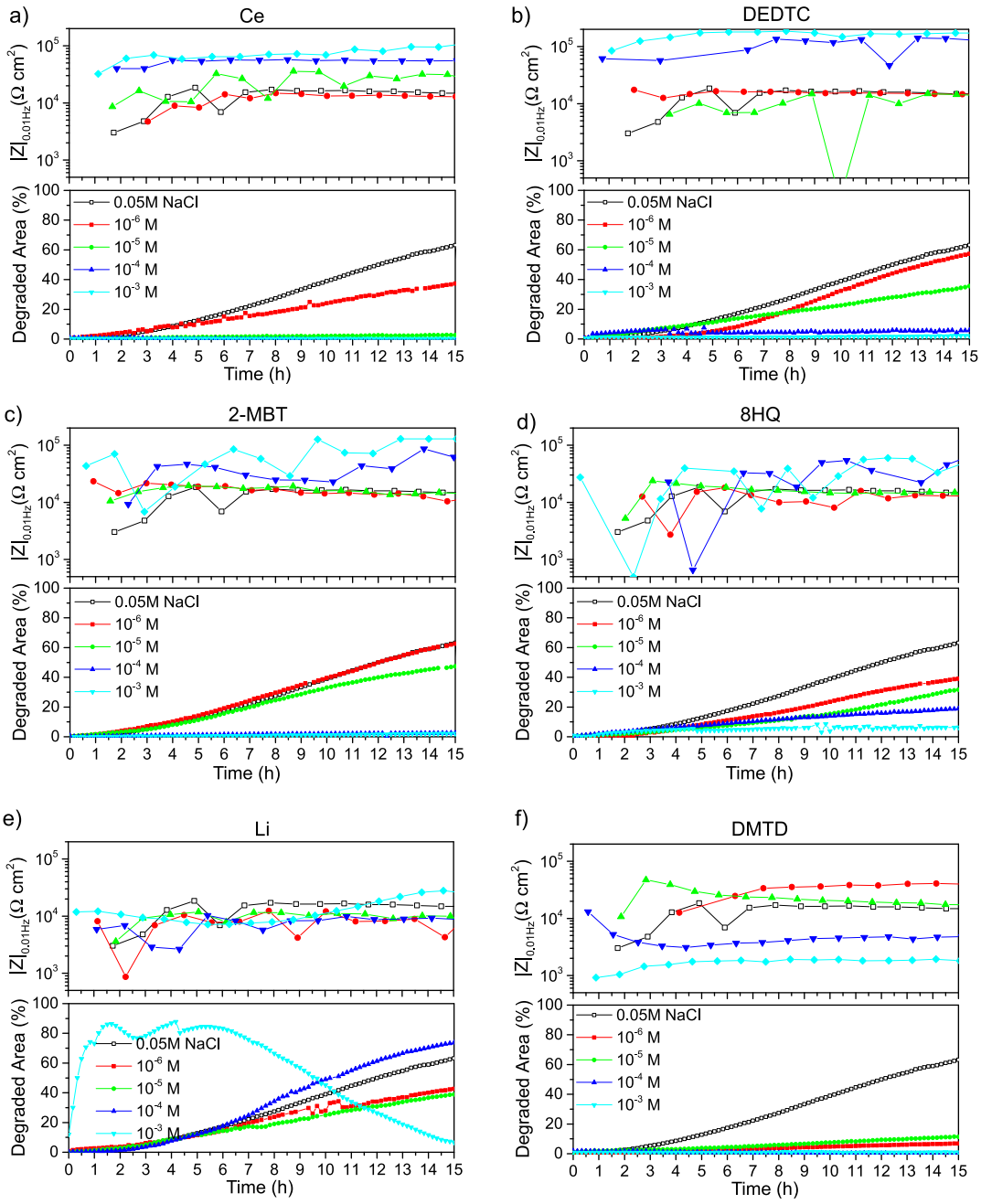

Fig. 7. Time evolution of the total impedance |Z| at a frequency of 0.01 Hz and the calculated optically-detectable degraded area in percentage for AA2024-T3 during 15 h immersion in 0.05 M NaCl electrolyte containing different concentrations of inhibitor Ce (a), DEDTC (b), 2-MBT (c), and 8HQ (d), Li (e), DMTD (f). (For interpretation of the references to colour in this figure legend, the reader is referred to the Web version of this article.)

suggesting that impedance alone might not always be enough to evaluate inhibition and highlighting the need for in situ optical-electrochemical analysis as proposed here.

In order to compare the inhibiting classification given by the electrochemical and optical analysis the total impedance at 0.01 Hz can be plot against the degraded area surface coverage for a given immersion time. Fig. 8 shows such a plot at 15 h immersion in 0.05 M NaCl with all the inhibitor concentrations studied (10^{-3} M up to 10^{-6} M).

From this figure it becomes evident that inhibitors showing a high total impedance at 0.01 Hz are always accompanied by a low degraded area, indicating good corrosion-protection both electrochemically and optically. On the contrary, inhibitors that show a lower total impedance lower than the non-inhibited system do not necessarily result in a high degraded area, as is the case for DMTD. Based on these results it can be concluded that the optical analysis and quantification of the degraded area evolution is a powerful tool to identify and quantify corrosion inhibiting while the electrochemical impedance analysis can result in subjective interpretations as function of the inhibitor type.

3.2.2. Local spatial-resolved evaluation

Fig. 9 shows the colour plots of AA2024-T3 immersed for 15 h in 0.05 M NaCl containing inhibitors at different concentrations. A

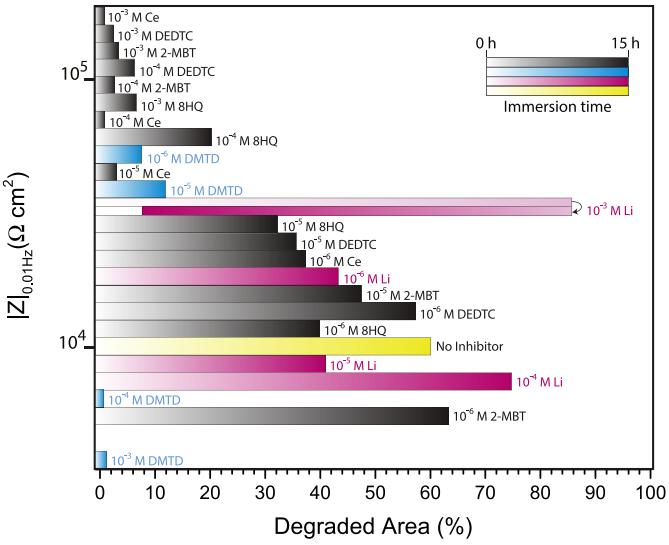

Fig. 8. Time-evolution of the degradation area of AA2024-T3 in 0.05 M NaCl solutions containing corrosion inhibitors against the total impedance at 0.01 Hz categorized per decade. The three overall inhibitor groups are indicated for Ce, DEDTC, 2MBT and 8HQ (black), Li (Margenta), and DMTD (Cyan) and additionally the non-inhibited sample (Yellow). (For interpretation of the references to colour in this figure legend, the reader is referred to the Web version of this article.)

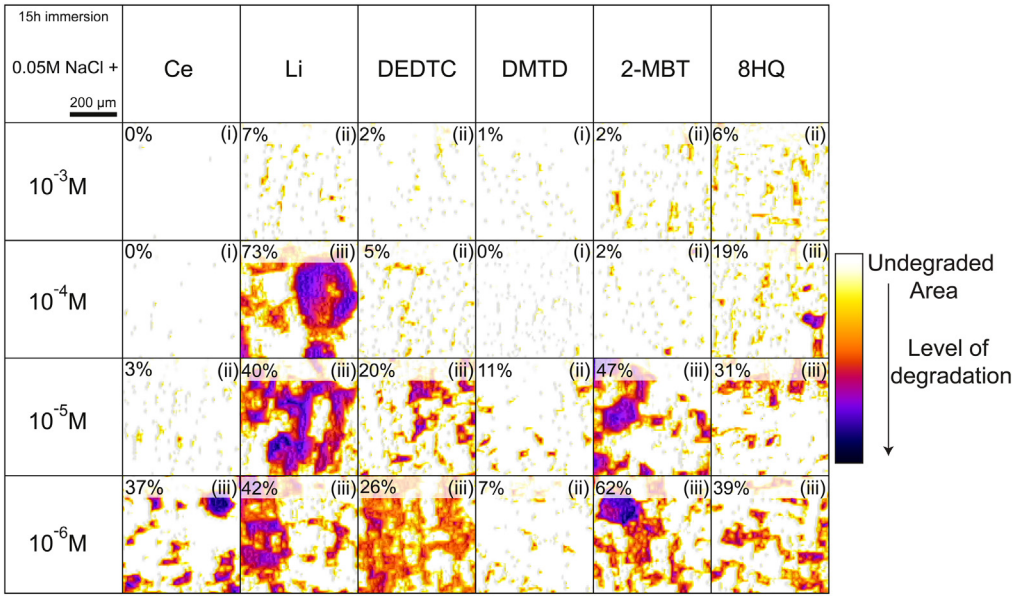

Fig. 9. Colour plots of the micrographs obtained from the optical analysis for AA2024 after 15 h immersion in 0.05 M NaCl containing corrosion inhibitors at different concentrations. The values in the micrographs represent the total degraded area in percentage, and the presence of (i) no visual surface-features, (ii) red spots between 5 and 30 µm in diameter, and (iii) purple domes and oxide-deposits. (For interpretation of the references to colour in this figure legend, the reader is referred to the Web version of this article.)

time-lapse of the optical images during 15 h of immersion can also be viewed in the Movie SI 6.

In Fig. 9 surface features related to local corrosion processes can be seen whereby the total degraded area given in the upper left corner is calculated over a 2 mm^2 exposed surface corresponding to the values shown in Figs. 7 and 8 after 15 h immersion. The micrographs for the 2 mm^2 exposed surface can be found in SI 7. Based on the type and amount of surface-degradation, the degree of inhibition can be related to the corrosion-features typically identified on non-inhibited AA2024-T3 in 0.05 M NaCl (Fig. 6). The inhibitor-concentration micrographs marked with an (i) in Fig. 9 show the absence of corrosion-related surface features. This suggests that the inhibitors (Ce and DMTD) are able to stop the corrosion-processes within the first 30 min of immersion, preventing trenching and pit-initiation during the next 15 h of immersion. The inhibitor-concentration micrographs marked with a (ii) in Fig. 9 show moderate degrees of surface degradation whereby the features are similar to those observed for meta-stable pit-formation (red spots between 5 and 30 µm) combined with a total degraded surface between 2% and 11%. Although these features can be related to the local deposition of inhibitor-products at the surface, the disappearance of features related to co-operative corrosion generally detected after several hours of immersion as seen in Fig. 5 (purple domes and oxide-deposits) suggests that local corrosion processes have been significantly supressed in those inhibitor-concentration combinations marked with (i) and (ii). The inhibitor-

concentration micrographs marked with (iii) in Fig. 9 show surface features generally taking place after several hours immersion without the presence of inhibition (Fig. 5) thereby suggesting the appearance of co-operative corrosion processes or, in the case of Li, massive surface-etching even in the presence of inhibitor.

4. Conclusion

A combined optical-electrochemical technique is proposed as inexpensive and simple method for the evaluation of corrosion and corrosion inhibition. For the proof of concept the data collection and analysis protocol were developed and used to study corrosion and corrosion inhibition of AA2024-T3. Three different corrosion stages were identified using time-dependent surface variations quantified by optical analysis and low frequency total impedance. Further analysis of the optical micrographs enabled the visualization and identification of time-dependent surface-related corrosion features corresponding to intermetallic corrosion (e.g. trenching and meta-stable pitting) and co-operative corrosion (e.g. corrosion-rings, domes and surface-oxides) typically only identified by SEM or ex-situ optical microscopy studies. The same optical-electrochemical technique and protocol was used to study six corrosion inhibitors. The optical analysis protocol allowed calculating inhibition kinetics, identifying three different inhibitor-concentration dependent behaviours and visualizing the presence or absence of local corrosion features depending on the level of inhibition with high spatial and temporal resolution. In terms of inhibitor behaviour it was found that both $Ce(NO_3)_3$ and DMTD are robust inhibitors showing little concentration dependency and able to prevent the initiation of early-stage corrosion within 30 min of immersion as well as long term immersion. The use of optical analysis with high local resolution allowed determining the high level of protection by DMTD despite its low impedance values. Li_2CO_3 on the other hand showed a very high concentration and time dependency up to the point that short immersion times and low concentrations lead to high degradation levels as measured with the optical evaluation. The results highlight the high potential of in-situ optical analysis under immersion combined with electrochemical analysis. In essence, the optical analysis could be used as a complementary technique to clarify EC models for corrosion and inhibitor action. Although the measurements have been performed on aluminium alloy AA2024-T3 with the used of EIS, the used opto-electrochemical setup and protocol analysis can easily be adapted to improve the interpretation of electrochemical signals from other electrochemical tests such as electrochemical noise as well as to follow surface related phenomena on other metal substrates with high spatio-temporal resolution without the need of extensive post-mortem analysis.

Acknowledgements

The authors would like to acknowledge Prof. Sybrand van der Zwaag for his continued support and constructive discussions, and Angelique Chabanon for the help with the opto-electrochemical experiments. The authors also acknowledge the Faculty of Aerospace Engineering at the Delft University of Technology, The Netherlands for the financial support.

Appendix A. Supplementary data

Supplementary data to this article can be found online at https://doi.org/10.1016/j.electacta.2018.10.018.

References

[1] M.E. Orazem, B. Tribollet, History of impedance spectroscopy, in: Electrochem. Impedance Spectrosc, second ed., John Wiley & Sons, 2017 xlii–xlvii. Incorporated.
[2] H. Unz, Oliver Heaviside (1850-1925), IEEE Trans. Educ. 6 (1963) 30–33.
[3] I. Yavetz, From Obscurity to Enigma: the Work of Oliver Heaviside, first ed., Birkhäuser Basel, Basel, 1995, pp. 1872–1889, https://doi.org/10.1007/978-3-0348-0177-5.
[4] D.D. Macdonald, Reflections on the history of electrochemical impedance spectroscopy, Electrochim. Acta 51 (2006) 1376–1388, https://doi.org/10.1016/j.electacta.2005.02.107.
[5] W. Tait, K. Handrich, S. Tait, J. Martin, Analyzing and interpreting electrochemical impedance spectroscopy data from internally coated steel aerosol containers, in: J. Scully, D. Silverman, M. Kendig (Eds.), Electrochem. Impedance Anal. Interpret, ASTM International, West Conshohocken, 1993, pp. 428–437.
[6] E.L. Ferrer, A.P. Rollon, H.D. Mendoza, U. Lafont, S.J. Garcia, Double-doped zeolites for corrosion protection of aluminium alloys, Microporous Mesoporous Mater. 188 (2014) 8–15, https://doi.org/10.1016/J.Micromeso.2014.01.004.
[7] T.H. Muster, H. Sullivan, D. Lau, D.L.J. Alexander, N. Sherman, S.J. Garcia, T.G. Harvey, T.A. Markley, A.E. Hughes, P.A. Corrigan, A.M. Glenn, P.A. White, S.G. Hardin, J. Mardel, J.M.C. Mol, A combinatorial matrix of rare earth chloride mixtures as corrosion inhibitors of AA2024-T3: optimisation using potentiodynamic polarisation and EIS, Electrochim. Acta 67 (2012) 95–103, https://doi.org/10.1016/J.Electacta.2012.02.004.
[8] F. Francisco, J. Bisquert, Influence of electrolyte in transport and recombination in dye-sensitized solar cells studied by impedance spectroscopy, Sol. Energy Mater. Sol. Cells 87 (2005) 117–131, https://doi.org/10.1016/j.solmat.2004.07.017.
[9] F.E.-T. Heakal, S. Haruyama, Impedance studies of the inhibitive effect of benzotriazole on the corrosion of copper in sodium chloride medium, Corrosion Sci. 20 (1980) 887–898.
[10] A.M. Glenn, T.H. Muster, C. Luo, X. Zhou, G.E. Thompson, A. Boag, A.E. Hughes, Corrosion of AA2024-T3 Part III: propagation, Corrosion Sci. 53 (2011) 40–50, https://doi.org/10.1016/j.corsci.2010.09.035.
[11] S.R.K. Malladi, F.D. Tichelaar, Q. Xu, M.Y. Wu, H. Terryn, J.M.C. Mol, F. Hannour, H.W. Zandbergen, Quasi in situ analytical TEM to investigate electrochemically induced microstructural changes in alloys: AA2024-T3 as an example, Corrosion Sci. 69 (2013) 221–225, https://doi.org/10.1016/j.corsci.2012.12.006.
[12] S.J. Garcia, T.A. Markley, J.M.C. Mol, A.E. Hughes, Unravelling the corrosion inhibition mechanisms of bi-functional inhibitors by EIS and SEM–EDS, Corrosion Sci. 69 (2013) 346–358, https://doi.org/10.1016/j.corsci.2012.12.018.
[13] P.J. Denissen, S.J. Garcia, Cerium-loaded algae exoskeletons for active corrosion protection of coated AA2024-T3, Corrosion Sci. 128 (2017) 164–175, https://doi.org/10.1016/j.corsci.2017.09.019.
[14] D. Snihirova, S.V. Lamaka, P. Taheri, J.M.C. Mol, M.F. Montemor, Comparison of the synergistic effects of inhibitor mixtures tailored for enhanced corrosion protection of bare and coated AA2024-T3, Surf. Coating. Technol. 303 (2016) 342–351, https://doi.org/10.1016/j.surfcoat.2015.10.075.
[15] A. Boag, A.E. Hughes, A.M. Glenn, T.H. Muster, D. McCulloch, Corrosion of AA2024-T3 Part I: localised corrosion of isolated IM particles, Corrosion Sci. 53 (2011) 17–26, https://doi.org/10.1016/j.corsci.2010.09.009.
[16] S.M. Ghahari, A.J. Davenport, T. Rayment, T. Suter, J. Tinnes, C. Padovani, J.A. Hammons, M. Stampanoni, F. Marone, R. Mokso, In situ synchrotron X-ray micro-tomography study of pitting corrosion in stainless steel, Corrosion Sci. 53 (2011) 2684–2687, https://doi.org/10.1016/j.corsci.2011.05.040.
[17] S.J. Garcia, X. Wu, S. Van Der Zwaag, A combined electrochemical impedance spectroscopy and X-ray-computed tomography study of the effect of a silyl ester on delamination and underfilm pit formation in a coated AA7050 sample, Corrosion 70 (2014) 475–482.
[18] V. Shkirskiy, A.D. King, O. Gharbi, P. Volovitch, J.R. Scully, K. Ogle, N. Birbilis, Revisiting the Electrochemical Impedance Spectroscopy of Magnesium with Online Inductively Coupled Plasma Atomic Emission Spectroscopy, 75005, 2015, pp. 536–539, https://doi.org/10.1002/cphc.201402666.
[19] E.M. Sherif, R.M. Erasmus, J.D. Comins, In situ Raman spectroscopy and electrochemical techniques for studying corrosion and corrosion inhibition of iron in sodium chloride solutions, Electrochim. Acta 55 (2010) 3657–3663, https://doi.org/10.1016/j.electacta.2010.01.117.
[20] M.L. Zheludkevich, R. Serra, M.F. Montemor, K.A. Yasakau, I.M.M. Salvado, M.G.S. Ferreira, Nanostructured sol-gel coatings doped with cerium nitrate as pre-treatments for AA2024-T3 Corrosion protection performance, Electrochim. Acta 51 (2005) 208–217, https://doi.org/10.1016/j.electacta.2005.04.021.
[21] S.J. Xia, R. Yue, R.G. Rateick Jr., V.I. Birss, Electrochemical studies of AC/DC anodized Mg alloy in NaCl solution, J. Electrochem. Soc. 151 (2004) B179–B187, https://doi.org/10.1149/1.1646139.
[22] H. Yasuda, Q.S. Yu, M. Chen, Interfacial factors in corrosion protection: an EIS study of model systems, Prog. Org. Coating 41 (2001) 273–279, https://doi.org/10.1016/S0300-9440(01)00142-4.
[23] L. Wen, Y. Wang, Y. Zhou, L. Guo, J.H. Ouyang, Microstructure and corrosion

resistance of modified 2024 Al alloy using surface mechanical attrition treatment combined with microarc oxidation process, Corrosion Sci. 53 (2011) 473–480, https://doi.org/10.1016/j.corsci.2010.09.061.
[24] G.O. Ilevbare, J.R. Scully, J. Yuan, R.G. Kelly, Inhibition of pitting corrosion on aluminum alloy 2024-T3: effect of soluble chromate additions vs chromate conversion coating, Corrosion 56 (2000) 227–242, https://doi.org/10.5006/1.3287648.
[25] D. Battocchi, A.M. Simões, D.E. Tallman, G.P. Bierwagen, Electrochemical behaviour of a Mg-rich primer in the protection of Al alloys, Corrosion Sci. 48 (2006) 1292–1306, https://doi.org/10.1016/j.corsci.2005.04.008.
[26] K.A. Yasakau, M.L. Zheludkevich, S.V. Lamaka, M.G.S. Ferreira, Mechanism of corrosion inhibition of AA2024 by rare-earth compounds, J. Phys. Chem. B 110 (2006) 5515–5528, https://doi.org/10.1021/Jp0560664.
[27] A. Boag, R.J. Taylor, T.H. Muster, N. Goodman, D. McCulloch, C. Ryan, B. Rout, D. Jamieson, A.E. Hughes, Stable pit formation on AA2024-T3 in a NaCl environment, Corrosion Sci. 52 (2010) 90–103, https://doi.org/10.1016/j.corsci.2009.08.043.
[28] N. Birbilis, R.G. Buchheit, Investigation and discussion of characteristics for intermetallic phases common to aluminum alloys as a function of solution pH, J. Electrochem. Soc. 155 (2008) C117–C126, https://doi.org/10.1149/1.2829897.
[29] F.M. Queiroz, M. Magnani, I. Costa, H.G. de Melo, Investigation of the corrosion behaviour of AA 2024-T3 in low concentrated chloride media, Corrosion Sci. 50 (2008) 2646–2657, https://doi.org/10.1016/j.corsci.2008.06.041.
[30] M. Shao, Y. Fu, R. Hu, C. Lin, A study on pitting corrosion of aluminum alloy 2024-T3 by scanning microreference electrode technique, Mater. Sci. Eng. 344 (2003) 323–327, https://doi.org/10.1016/S0921-5093(02)00445-8.
[31] R.G. Buchheit, R.P. Grant, P.F. Hiava, B. Mckenzie, G.L. Zender, Local Dissolution Phenomena Associated with S Phase (Al2CuMg) Particles in Aluminum Alloy 2024-T3, vol, 144, 1997, pp. 2621–2628.
[32] A.E. Hughes, A. Boag, A.M. Glenn, D. McCulloch, T.H. Muster, C. Ryan, C. Luo, X. Zhou, G.E. Thompson, Corrosion of AA2024-T3 Part II: Co-operative corrosion, Corrosion Sci. 53 (2011) 27–39, https://doi.org/10.1016/j.corsci.2010.09.030.
[33] C.-M.M. Liao, J.M. Olive, M. Gao, R.P. Wei, In-situ monitoring of pitting corrosion in aluminum alloy 2024, Corrosion 54 (1998) 451–458, https://doi.org/10.5006/1.3284873.
[34] C.-M.M. Liao, R.P. Wei, Galvanic Coupling of Model Alloys to Aluminum — a Foundation for Understanding Particle-Induced Pitting in Aluminum Alloys, vol. 45, 1999, pp. 881–888.
[35] N. Dimitrov, J.A. Mann, M. Vukmirovic, K. Sieradzki, Dealloying of Al2CuMg in alkaline media, J. Electrochem. Soc. 147 (2000) 3283–3285, https://doi.org/10.1149/1.1393896.
[36] A. Hughes, T.H. Muster, A. Boag, A.M. Glenn, C. Luo, X. Zhou, G.E. Thompson, D. McCulloch, Co-operative corrosion phenomena, Corrosion Sci. 52 (2010) 665–668, https://doi.org/10.1016/j.corsci.2009.10.021.
[37] R.L. Twite, G.P. Bierwagen, Review of alternatives to chromate for corrosion protection of aluminum aerospace alloys, Prog. Org. Coating 33 (1998) 91–100, https://doi.org/10.1016/S0300-9440(98)00015-0.
[38] C.M. Rangel, M.A. Travassos, The passivation of aluminium in lithium carbonate/bicarbonate solutions, Corrosion Sci. 33 (1992) 327–343.
[39] P. Visser, M. Meeusen, Y. Gonzalez-Garcia, H. Terryn, J.M.C. Mol, Electrochemical evaluation of corrosion inhibiting layers formed in a defect from lithium-leaching organic coatings, J. Electrochem. Soc. 164 (2017) 396–406, https://doi.org/10.1149/2.1411707jes.
[40] G. Williams, A.J. Coleman, H.N. McMurray, Inhibition of Aluminium Alloy AA2024-T3 pitting corrosion by copper complexing compounds, Electrochim. Acta 55 (2010) 5947–5958, https://doi.org/10.1016/j.electacta.2010.05.049.
[41] M. Finšgar, D. Kek Merl, An electrochemical, long-term immersion, and XPS study of 2-mercaptobenzothiazole as a copper corrosion inhibitor in chloride solution, Corrosion Sci. 83 (2014) 164–175, https://doi.org/10.1016/j.corsci.2014.02.016.
[42] S. Ridler, T.W. Calvard, Picture thresholding using an iterative slection method, IEEE Trans. Syst. Man Cybern. 8 (1978) 630–632, https://doi.org/10.1109/TSMC.1978.4310039.
[43] S.K. Poznyak, J. Tedim, L.M. Rodrigues, A.N. Salak, M.L. Zheludkevich, L.F. Dick, M.G. Ferreira, Novel inorganic host layered double hydroxides intercalated with guest organic inhibitors for anticorrosion applications, ACS Appl. Mater. Interf. 1 (2009) 2353–2362, https://doi.org/10.1021/am900495r.
[44] W. Chen, H.Q. Luo, N.B. Li, Inhibition effects of 2,5-dimercapto-1,3,4-thiadiazole on the corrosion of mild steel in sulphuric acid solution, Corrosion Sci. 53 (2011) 3356–3365, https://doi.org/10.1016/j.corsci.2011.06.013.